Correspondence to:
J. R. Jordan,
jamrda26@bas.ac.uk

Modeling ice-ocean interaction in ice-shelf crevasses

James R. Jordan[1], Paul R. Holland[1], Adrian Jenkins[1], Matthew D. Piggott[2,3], and Satoshi Kimura[1]

[1]British Antarctic Survey, Cambridge, UK, [2]Applied Modelling and Computation Group, Department of Earth Science and Engineering, Imperial College London, London, UK, [3]Grantham Institute for Climate Change, Imperial College London, London, UK

Abstract Ocean freezing within ice-shelf basal crevasses could potentially act as a stabilizing influence on ice shelves; however, ice-ocean interaction and ocean dynamics within these crevasses are as yet poorly understood. To this end, an idealized 2-D model of an ice-shelf basal crevasse has been developed using Fluidity, a finite-element ocean model using an unstructured mesh. A simple model of frazil ice formation and deposition has been incorporated into Fluidity to better represent the freezing process. Model results show two different flow regimes, dependent on the amount of freezing in the crevasse: one driven by freezing at the top of the crevasse and the other by the ingress of meltwater from outside the crevasse. In the first, freezing at the top of the crevasse leads to the formation of an unstable overturning circulation due to the rejection of dense, salty water. In the second, a buoyant layer is formed along the sides and roof of the crevasse, stratifying the water column. Frazil ice precipitation is found to be the dominant freezing process at the top of the basal crevasse in the freeze-driven case, with direct freezing being dominant in the melt-driven case. In both cases, melting occurs lower down on the walls of the crevasse due to the strong overturning circulation. The freezing in ice-shelf crevasses and rifts is found to be highly dependent upon ocean temperature, providing a stabilizing influence on ice shelves underlain by cold waters that is not present elsewhere.

1. Introduction

The most profound changes in the Antarctic Ice Sheet currently result from glacier dynamics at ocean margins [*Pritchard et al.*, 2009], where the ice streams flow out over the ocean to form large floating ice shelves [*Pritchard et al.*, 2012; *Rignot et al.*, 2013]. Over the last few decades ice shelves on the Antarctic Peninsula have retreated, and this is thought to be associated with atmospheric warming [*Vaughan and Doake*, 1996]. As well as a general reduction in Antarctic Peninsula ice-shelf area (roughly 28,000 km^2 over the last 30 years) [*Cook and Vaughan*, 2010] there have been dramatic collapses of individual ice shelves over a short time period, such as Larsen A in 1995 and Larsen B in 2002. The final collapse of these ice shelves was a result of increased surface meltwater production, leading to fracturing of the ice-shelf into individual blocks of ice [*Scambos et al.*, 2000]. These dramatic collapses are believed to be a result of thinning due to atmospheric warming and perhaps increased basal melting [*Shepherd et al.*, 2003; *Glasser and Scambos*, 2008; *Holland et al.*, 2011]. The collapse of an ice-shelf has little direct impact on sea level, but the resulting reduction in buttressing of inshore glaciers can enhance the flow of outlet glaciers from the continental ice sheet and thus cause sea-level rise [*Rignot et al.*, 2004].

It is possible for the ocean to freeze onto the underside of ice shelves. Because the freezing temperature decreases with increasing pressure, water at the surface freezing point melts ice shelves at depth, generating meltwater, which is cooler and fresher than the surrounding water. The density of water at temperatures near the freezing point is determined mainly by its salinity, and therefore, the meltwater is lighter than the surrounding water. As a result, the meltwater rises and may become supercooled due to the pressure release (Figure 1) and form "marine" ice on the base of the ice shelf [*Robin*, 1979]. As well as direct freezing onto the ice base, small disk-shaped frazil ice crystals (with radii in the range 0.01–10 mm) form in a turbulent body of water when it becomes supercooled, and these can deposit onto the ice [*Daly*, 1984].

Basal crevasses can form on the underside of ice shelves allowing seawater to penetrate the ice shelf and rupture the ice up to the level at which longitudinal stress acting to open the crevasse is sufficiently
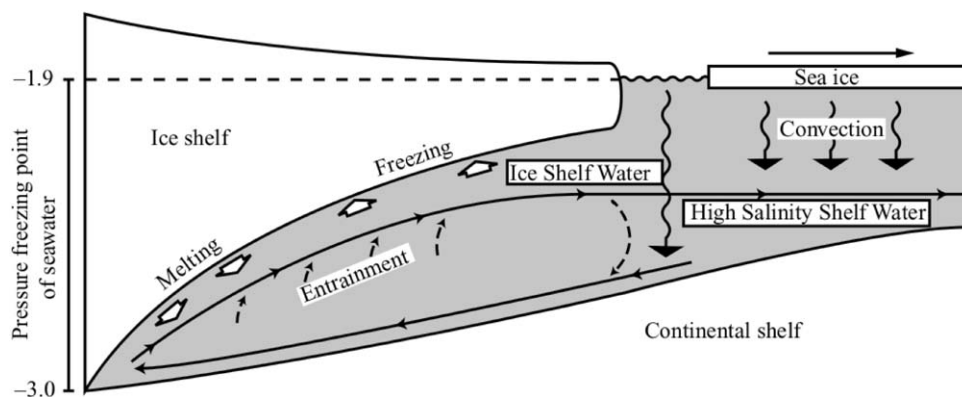
Figure 1. Schematic diagram of the thermohaline circulation under an ice shelf [*Holland and Feltham*, 2005]. The formation of sea ice generates high-salinity shelf water, which sinks down the continental shelf and melts the ice shelf at its grounding line. The fresh meltwater released initiates an Ice Shelf Water plume, which becomes supercooled as it rises due to the pressure release and thus deposits ice at shallower depths.

balanced by the confining presence of the surrounding ice [*Jezek*, 1984]. An initial flaw in the base of the ice shelf will only propagate upward if it exceeds a critical width, typical in the order of 0.9–1.7 m [*Rist et al.*, 2002]. The final crevasses can be many kilometers long and several hundred meters wide and deep [*Luckman et al.*, 2012; *McGrath et al.*, 2012a, 2012b]. Basal crevasses have been observed on, among others, the Larsen [*Swithinbank*, 1977], Ross [*Jezek and Bentley*, 1983] and Fimbul [*Humbert and Steinhage*, 2011] ice shelves, and they are a fairly common feature. Crevasses observed by *McGrath et al.* [2012a] were found to have their greatest depth and smallest width near their origin, with the crevasses becoming shallower and wider as they propagate toward the calving front. *McGrath et al.* [2012a] suggest that this change in crevasse geometry is a combination of marine ice accretion at the top of the crevasse and bending stresses within the ice shelf, with the latter being the dominant process. Another possible explanation is the formation of a melt-driven ocean convection cycle within the crevasse itself, with melting happening low down on the crevasse walls and marine ice accretion higher up [*Khazendar and Jenkins*, 2003].

The presence of basal crevasses will modify local stresses in the ice, potentially affecting ice-shelf stability [*Jezek*, 1984; *Holland et al.*, 2009]. They also increase the basal surface area over which melting occurs and allow heat exchange between the ice and ocean deep within the ice column, potentially speeding up melting [*Hellmer and Jacobs*, 1992]. Marine ice may form at the top of basal crevasses because the pressure freezing point difference between the base and top of the crevasse drives a thermohaline circulation within it [*Khazendar and Jenkins*, 2003]. Bands of marine ice, potentially formed in this way, have been observed in Larsen Ice Shelf, and this marine ice appears to play a role in stabilizing the ice shelf [*Holland et al.*, 2009]. Marine ice is comparatively warmer than meteoric ice and is therefore more likely to deform rather than fail in response to stress. There is evidence that bands of marine ice act as a barrier to the propagation of rifts [*Holland et al.*, 2009]. Marine ice has also been shown to heal rifts by binding their edges together with deformable material [*Rignot and MacAyeal*, 1998].

Obtaining observations of the physical conditions beneath ice shelves is challenging, and there are particularly few observations of ocean conditions within basal crevasses. Temperature and salinity profiles measured in the Jutulgryta rift, a 340 m wide and 260 m deep rift on the Fimbulisen Ice Shelf, were obtained by *Orheim et al.* [1990] (reprinted by *Khazendar and Jenkins* [2003]). A rift differs from a crevasse in that it extends vertically throughout the entire ice column; however, as the Jutulgryta rift was "capped" by approximately 40 m of sea ice, marine ice, and ice debris it is assumed to be a fair approximation to a basal crevasse. Ocean properties were vertically uniform within the rift, with a 60 m thick layer of supercooled water and frazil ice at the top. Approximately 2 m of ice accumulation occurred at the top of the rift over the course of 2 years [*Østerhus and Orheim*, 1992; *Khazendar and Jenkins*, 2003], and the average flow velocity past the crevasse was of the order of 2.5 cm s^{-1} [*Orheim et al.*, 1990].

Previous studies of ice-shelf basal crevasses have mainly considered the formation and evolution of the crevasse itself rather than ocean flow and freezing within it [e.g., *Luckman et al.*, 2012; *McGrath et al.*, 2012a, 2012b]. Ocean modeling work has generally been at larger scales, considering ice-shelf cavities as a whole
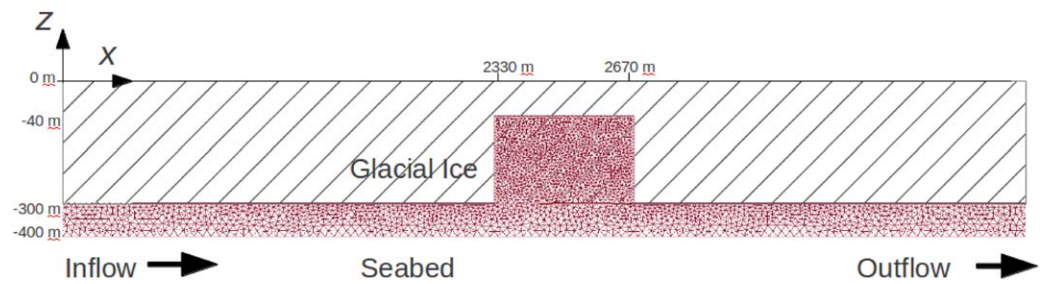
Figure 2. Model mesh. Resolution varies from 5 m inside the basal crevasse to 20 m outside. A flow past the crevasse is imposed from left to right.

rather than individual basal crevasses. *Khazendar and Jenkins* [2003] modeled in one (vertical) dimension the freezing rate within a basal crevasse and the impact this has on the water inside. However, the 1-D nature of their model limited the representation of ocean dynamics.

In this study, we use a nonhydrostatic finite-element ocean model with a flexible unstructured mesh (Fluidity) [*Piggott et al.*, 2008] to study ocean dynamics and ice-ocean interaction (including frazil ice production and deposition) in an idealized 2-D basal crevasse. The use of a nonhydrostatic finite-element model was deemed to be well suited to the irregular geometry, high aspect ratio, and multiphase physics of an ice-shelf basal crevasse. By means of a sensitivity study we aim to identify the key factors affecting marine ice production in basal crevasses.

2. Model and Experimental Design

2.1. Ocean Model
Ice shelves have previously been incorporated into Fluidity, and the model used to study ocean dynamics and ice-ocean interaction beneath ice shelves [*Kimura et al.*, 2013]. In this study, the ocean dynamics are governed by the 2-D nonhydrostatic Navier-Stokes equations under the Boussinesq approximation in a non-rotating Cartesian coordinate system (x, z). The domain considered is relatively small, so we neglect the Coriolis effect. The density (ρ) is considered constant except in the buoyancy term, which uses a linear equation of state modified to include the effects of frazil ice

$$\rho = \rho_0(1 - \alpha(T - T_0) + \beta(S - S_0))(1 - C) + \rho_i C, \tag{1}$$

where ρ is the density of the ice-seawater mixture, $\rho_0 = 1030$ kg m^{-3} is the reference density of seawater, $\alpha = 3.87 \times 10^{-5}$°C^{-1} is the thermal expansion coefficient, T is the temperature, $T_0 = -2$°C is the reference temperature, $\beta = 7.86 \times 10^{-4}$ psu^{-1} is the haline contraction coefficient, S is the salinity, $S_0 = 34.5$ psu is the reference salinity, $\rho_i = 920$ kg m^{-3} is the ice density, and C is the dimensionless frazil ice concentration (volume of ice per unit volume of ice-seawater mixture). Velocity and pressure are discretized within first-order discontinuous and second-order continuous function spaces, respectively (a so-called P1$_{DG}$–P2 finite-element pair), as described in *Cotter et al.* [2009]. Equations governing the conservation of heat, salt, and frazil ice concentration are discretized with a flux-limited control volume method [*Piggott et al.*, 2009]. All quantities are subject to a uniform, isotropic diffusivity/viscosity of 10^{-3} m^2 s^{-1}.

Our model domain has been chosen to represent the dimensions of the Jutulgryta rift, as this provides some ocean data for calibration purposes. The domain is a 2-D rectangular channel 5 km long in the streamwise (x) and 100 m in the vertical (z) directions, representing a section of the cavity beneath an ice shelf (Figure 2). The upper surface is considered glacial ice and the bottom seabed. An idealized basal crevasse 260 m wide by 340 m deep is placed in the middle of the ice shelf, making the water column thickness 440 m at its thickest. By using a finite-element ocean model we can increase the grid resolution in areas of interest while maintaining a coarser resolution elsewhere, reducing the computational expense. As such, mesh resolution is 20 m except in the crevasse, where a higher resolution of 5 m has been used. A time step of 5 s was used in all simulations in order to obtain a Courant number <1. An inflow enters the domain from the upstream side (left, $x = 0$) under steady Dirichlet boundary

conditions ($w = 0$, $u = U_{in}$, $T = T_{in}$, $S = S_{in}$ and $C = 0$) and leaves via the downstream side (right, $x = 5$ km) with zero-flux Neumann boundary conditions ($\partial u/\partial x = \partial w/\partial x = \partial T/\partial x = \partial S/\partial x = \partial C/\partial x = 0$). No-slip boundary conditions are applied in discretized space ("weakly applied") at the ice-shelf boundary and the seabed. Zero-flux conditions for heat, salt, and frazil are applied at the seabed. The thermodynamics of melting and freezing directly onto the ice-shelf-ocean boundary have already been implemented in Fluidity [*Kimura et al.*, 2013], and the ice pressure is represented by the "rigid lid" approximation. The model achieves steady state during the second week of run time, and all results have been time averaged over the third week.

2.2. Frazil Ice Dynamics

To better represent freezing in crevasses we add a frazil ice model to Fluidity. Frazil ice can be modeled by either representing the distribution of ice crystal sizes [*Smedsrud and Jenkins*, 2004; *Holland and Feltham*, 2006; *Galton-Fenzi et al.*, 2012] or more simply, by using a single representative size class [*Jenkins and Bombosch*, 1995]. The use of multiple size classes requires several additional tracers, so for computational simplicity the single-size-class frazil ice model of *Jenkins and Bombosch* [1995] has been incorporated into Fluidity for this study. This is justified on the grounds that we seek a basic qualitative study of the effect of frazil ice in crevasses, and we also perform a full assessment of the sensitivity of our results to the frazil size selected.

Fluidity already has a sediment model (S. Parkinson, unpublished manuscript, 2013) so we treat frazil ice in the model in a manner akin to a sediment with a negative submerged specific gravity and sinking velocity. Frazil ice has submerged specific gravity $R = (\rho_i - \rho_0)/\rho_0$, and the frazil rise velocity w_i relative to the moving fluid is approximated by frazil's buoyant drift velocity in still water [*Gosink and Osterkamp*, 1983]:

$$w_i^2 = \frac{4Rgr\epsilon}{C_d}, \tag{2}$$

where r is the chosen radius of frazil ice disks, $g = 9.81$ m s^{-2} is the acceleration due to gravity, and $\epsilon = 1/16$ is the aspect ratio of the frazil ice disk [*Clark and Doering*, 2006]. The drag coefficient C_d varies considerably with the disk Reynolds number, defined as

$$Re = \frac{w_i 2r}{v}, \tag{3}$$

where $v = 1.95 \times 10^{-6}$ m^{2}s^{-1} is the kinematic viscosity of seawater. *Gosink and Osterkamp* [1983] used published experimental data on the drag coefficient of disks of varying sizes to determine the following empirical relationship:

$$\log_{10}(C_d) = 1.386 - 0.892 \log_{10}(Re) + 0.111(\log_{10}(Re))^2. \tag{4}$$

By using an iterative method an estimate for w_i for a given crystal radius can be calculated from (2–4).

The total flux through an ice boundary (here the underside of the ice shelf and the walls and top of the crevasse), and hence the frazil ice deposition rate, is calculated via

$$\frac{\partial \eta}{\partial t} = w_b C, \tag{5}$$

where η is the thickness of frazil ice in meters and w_b is the component of w_i normal to the boundary. Resuspension of frazil ice crystals has been ignored in this work, as it is assumed that the crystals will adhere to the ice boundary. The parameter w_b is orientated directly upward, so frazil cannot deposit onto vertical walls. Due to our use of "weakly applied" no-slip velocity boundary conditions, some flow normal to the ice-ocean boundaries is present as an artifact of the numerical solution. This creates a negligible amount of frazil ice deposition onto the walls of the crevasse, which has been ignored in our calculation of freeze rate. The rate of frazil deposition is combined with direct freezing [*Kimura et al.*, 2013] to give a total freeze rate.

2.3. Frazil Ice Thermodynamics

The growth of frazil ice acts as a heat and salt source in the temperature and salinity equations [*Jenkins and Bombosch*, 1995]. The ice-ocean interface at the edge of a frazil crystal is assumed to be at the freezing temperature, so the temperature and salinity are related by a linear expression for the pressure freezing point of seawater:

$$T_c = a S_c + b + c z_c, \tag{6}$$

where T_c and S_c are the temperature and salinity at the edge of the frazil ice crystal, the variable z_c represents the elevation, and a, b, and c are constants $-0.0573°C\ psu^{-1}$, $0.0832°C$, and $7.61 \times 10^{-4}\ °C\ m^{-1}$, respectively. Balancing heat and salt transfer through the frazil boundary layer with the latent heat and freshwater release of melting, we obtain

$$(1-C)\gamma_T^c (T - T_c)\frac{2C}{r} = \frac{L}{c_0} w', \tag{7}$$

$$(1-C)\gamma_S^c (S - S_c)\frac{2C}{r} = w' S_c, \tag{8}$$

where $L = 3.35 \times 10^5\ J\ kg^{-1}$ is the latent heat of ice fusion, $c_0 = 3974\ J\ kg^{-1}°C^{-1}$ is the specific heat capacity of sea water, w' (s^{-1}) is the melt rate of frazil ice volume per unit volume of mixture, and γ_T^c and γ_S^c are the ocean heat and salt transfer coefficients at the edge of frazil ice crystals. For transfer at the disk edges the appropriate length scale is the half-thickness of the disk [*Daly*, 1984], so we calculate the transfer coefficients as follows:

$$\gamma_T^c = \frac{Nu\kappa_T}{\varepsilon r}, \gamma_S^c = \frac{Nu\kappa_S}{\varepsilon r} \tag{9}$$

where $\kappa_T = 1.4 \times 10^{-7}\ m^2 s^{-1}$ is the molecular thermal diffusivity of seawater, $\kappa_S = 8 \times 10^{-10}\ m^2 s^{-1}$ the molecular haline diffusivity of seawater, and Nu is the dimensionless Nusselt number, and we assume $Nu = 1$.

This gives three equations and three unknown variables T_c, S_c, and w'. We can derive a quadratic expression for S_c by substituting (6) and (7) into (8) and then ignoring the solution that leads to a negative value for S_c. This can then be used to eliminate S_c from (8) and thus solve for w'. As these equations require some frazil to be present before any freezing can occur, a very small minimum concentration of frazil $(C_{min} = 5 \times 10^{-9})$ is assumed to be always present in the solution of (1)–(8). This background concentration is only used to determine frazil growth/melting and is not part of the frazil ice concentration conserved in the model, as in *Jenkins and Bombosch* [1995].

The formation of frazil ice provides a source of heat and salt, the full derivation of which is shown in *Holland and Feltham* [2006]. The full evolution of temperature and salinity within the seawater fraction is defined as

$$\frac{\partial T}{\partial t} + \underline{\mathbf{u}} \cdot \nabla T = k_T \nabla^2 T + w'\left(\frac{L}{c_0} + T - T_f\right), \tag{10}$$

$$\frac{\partial S}{\partial t} + \underline{\mathbf{u}} \cdot \nabla S = k_S \nabla^2 S - w' S \tag{11}$$

In both cases the second term on the right-hand side is the change due to frazil ice production.

3. Experimental Design

3.1. Model Calibration

Our model has been calibrated to reproduce the observed temperature and salinity profiles and freezing rate within the Jutulgryta rift. In particular, we sought to reproduce the observed 60 m of supercooling and
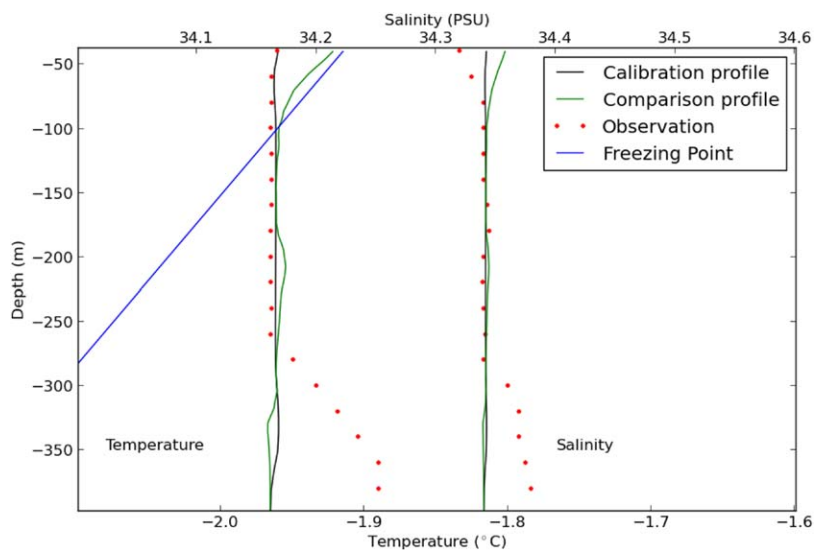
Figure 3. Model calibration. The modeled calibration profiles of salinity and temperature are shown in black, with comparison profiles shown in green and observations shown in red [*Orheim et al.*, 1990; *Khazendar and Jenkins*, 2003]. The freezing point (FP) of the inflow water is shown in blue.

1 m yr^{-1} freezing rate observed by *Orheim et al.* [1990]. In keeping with these observations, a constant initial temperature and salinity of $-1.965°$C and 34.34 psu has been used, with a constant 0.025 m s^{-1} inflow velocity with the same temperature and salinity as the initial conditions. Laboratory experiments find a mean frazil crystal radii in the range of 0.5–0.8 mm, [*Clark and Doering*, 2006], and baseline simulations with a frazil crystal radius of 0.75 mm best matched the rift observations.

When compared with observations (Figure 3) we are able to obtain a matching "calibration" temperature profile within the rift, including the 60 m of supercooled water at the top. Our salinity profile is a good fit over the majority of the crevasse, but we fail to obtain the freshening found at the top of the crevasse. Our model cannot reproduce the conditions observed outside the rift, below about 300 m, which are governed by the general circulation in the Fimbulsen cavity [*Hattermann et al.*, 2012]. The ocean modeled freezing rate was found to be 1.2 m yr^{-1} at the top of this profile. However, as shown by the results below, salinity and temperature within our modeled rift are not horizontally uniform, and so there will always be a considerable uncertainty in our calibration. Figure 3 also shows a "comparison" profile from elsewhere in the rift, and it is clear that in this location the supercooling has been taken up by frazil ice growth. At the top of this profile we have correspondingly larger freezing (of 16 m yr^{-1}). Since we only have measurements at a single location within the rift, the strongest calibration we can perform is to match that behavior of one location in the model. This calibrated setup has been used as a baseline case for a variety of sensitivity studies.

3.2. Sensitivity Studies

To gain a qualitative understanding of ocean processes and melting and freezing in ice-shelf crevasses, the effects of varying ocean temperature, inflow velocity, crystal radius, and crevasse geometry have been investigated in a set of sensitivity simulations. Specifically, these simulations have five different inflow and initial temperatures ($T1 = -1.89°$C, $T2 = -1.93°$C, $T3 = -1.965°$C (baseline), $T4 = -1.99°$C, and $T5 = -2.02°$C), five different inflow velocities ($U01 = 0.01$ m s^{-1}, $U025 = 0.025$ m s^{-1} (baseline), $U05 = 0.05$ m s^{-1}, $U10 = 0.1$ m s^{-1}, and $U20 = 0.20$ m s^{-1}), seven different mean crystal radii ($R025 = 0.25$ mm, $R065 = 0.65$ mm, $R070 = 0.7$ mm, $R075 = 0.75$ mm (baseline), $R080 = 0.8$ mm, $R085 = 0.85$ mm, and $R150 = 1.5$ mm), and five different crevasse geometries (260 m $\times$ 340 m (baseline), 260 m $\times$ 170 m, 130 m $\times$ 340 m, 260 m $\times$ 130 m crevasse with the cavity beneath the crevasse extended to 200 m, and a triangular crevasse 340 m at the base and 240 m in height). Simulations without the frazil ice and/or direct melting and freezing were also performed. The pressure decrease in the freezing temperature means that supercooling increases with height above seabed, so the temperature sensitivities were chosen to place the initial freezing point 20 m above the crevasse top ($T1$, i.e., no supercooling), 20 m below the crevasse top ($T2$), 60
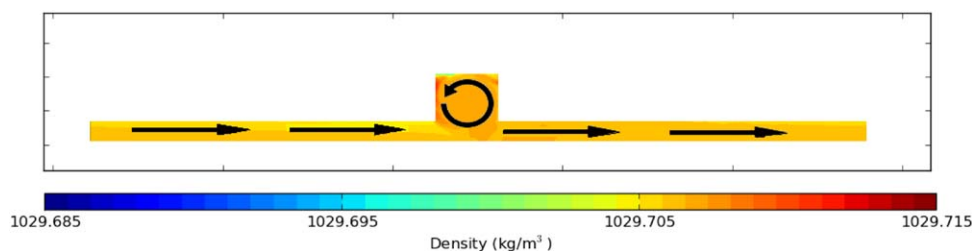
Figure 4. Overview of ocean dynamics for the whole domain in the baseline case. Flow enters from the left and leaves via the right. Meltwater rises into the crevasse and freezes on the top, creating a cold and saline dense layer. This dense layer enhances the overturning circulation within the crevasse.

m below the crevasse top (*T*3, baseline), 100 m below the crevasse top (*T*4), and 140 m below the crevasse top (*T*5), respectively. All settings except the one under investigation are held constant at their baseline values.

4. Results

4.1. Base Case

To provide a general overview, Figure 4 shows the density in the base case and a schematic illustration of the flow field. Flow enters from the left and is sufficiently warm to melt the base of the ice shelf outside the crevasse. Melting of the ice shelf provides a source of relatively cool and fresh meltwater which is less dense than the surrounding water. The meltwater rises up into the basal crevasse on its downstream side until, roughly 60 m from the top by construction, it reaches its freezing point and becomes supercooled. This supercooling leads to frazil ice formation within the water column, but not quickly enough to remove all the supercooling, so the supercooled water continues rising to the top of the crevasse, aided by the buoyancy of the frazil ice. Direct freezing occurs on the top and upper sides of the crevasse. Freezing, both direct and through frazil ice production, creates relatively warmer and saltier water by the release of latent heat and freshwater extraction. Some frazil ice accretes to the ice-shelf base, so the water left behind is denser than the water below it, creating an overturning circulation within the entire crevasse that is inherently statically unstable. The dense water descends down the upstream side of the crevasse and is then partially vented into the passing flow.

A closer inspection of the model results (Figure 5) shows that the time-averaged velocity of the circulation is greater than the inflow velocity, leading to greater rates of melting and freezing within the crevasse than outside it. The passing flow beneath the crevasse forces the overturning circulation to move in an anticlockwise direction (Figure 5a), with colder meltwater rising up on the downstream side, freezing at the top and then returning warmer on the upstream side (Figures 5a and 5b). Figure 5b shows contours of thermal driving $T^* = T - (aS + b + cz)$, which represent the local potential to freeze or melt ice (where the quantity in parentheses is the local freezing temperature). The thermal driving field leads to maximum frazil ice formation on the upstream side of the supercooled upper region, as the frazil crystals multiply in the horizontal flow across the crevasse (Figure 5c).This causes a significant lateral variation in the rate of ice deposition at the top of the crevasse, which accounts for the variation in model calibration results (Figure 3). This can be seen in Figure 5d, which shows the effect the calculated freeze rate would have on crevasse geometry if maintained for 5 years (geometry changes not included in model). This freezing is dominated by frazil ice, as shown in Table 1. Ice is also directly melted on the lower half of the crevasse sides, and refrozen higher up on the sides and at the top. This secondary effect would create a widening at the base of the crevasse and narrowing at the top, as predicted by *Khazendar and Jenkins* [2003].

4.2. Temperature Variation

In cases warmer than the baseline (Figures 6a and 6b), there is less or no-frazil and dense water production, so the circulation in the crevasse is primarily driven by meltwater as opposed to rejected brine. This leads to the buoyant meltwater rising up into the crevasse on the upstream side before leaving on the downstream. A simulation colder than the baseline has a greater amount of frazil growth within the crevasse and less melting outside (Figure 6d). This leads to a greater production of dense water at the top of the crevasse and a faster and less stable overturning circulation. When there is significant frazil ice production in the
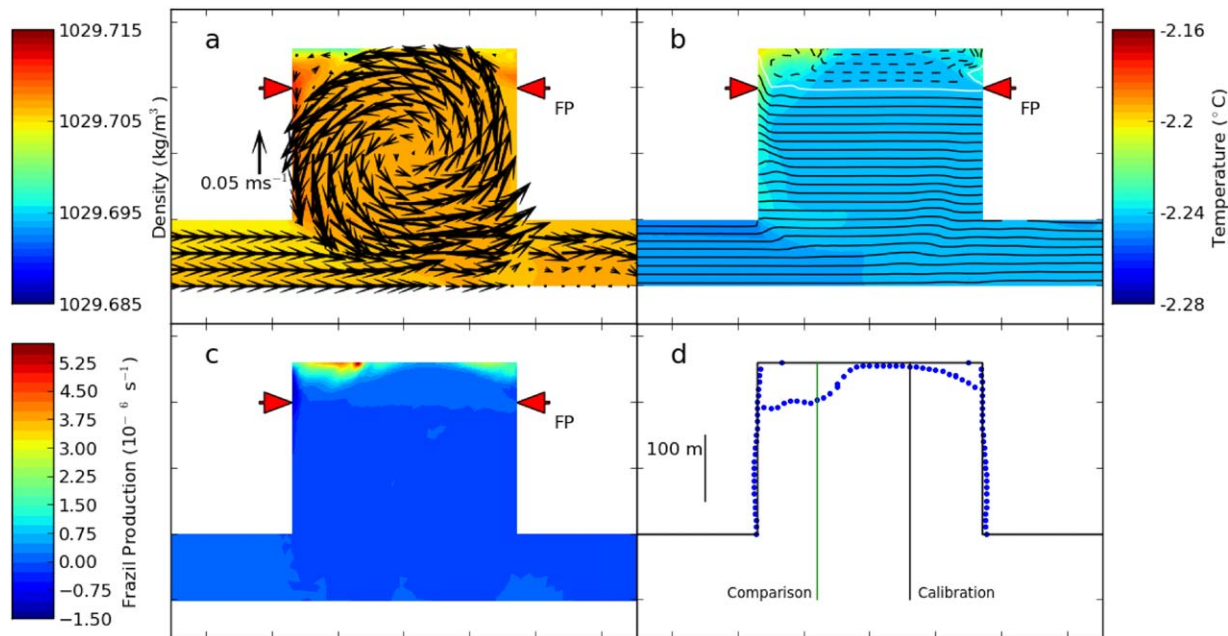
Figure 5. Baseline case showing (a) time-averaged (over the third week of simulation) mean density with mean velocity vectors, (b) mean temperature (colors) with mean thermal driving (contours), (c) mean frazil crystal production, and (d) change in crevasse geometry as a result of mean melt rate maintained for 5 years with the position of the calibration and comparison profiles shown in black and green, respectively. The white contour in Figure 5b is at zero thermal driving, while black contours are every 0.1° above and black dashed contours are every 0.01° below this point. The pressure-dependent FP of the water properties used for initial and inflow conditions is also shown.

crevasse the density of the water-ice mixture at the very top of the crevasse falls overall, even though the density of the water fraction has increased due to the greater salinity. In freezing-dominated cases, such as $T3$ and $T4$, frazil ice precipitation has a higher proportion of the freezing rate than direct freezing (Table 1).

Warmer cases (Figures 7a and 7b) have flatter thermal driving contours than the baseline case (Figure 7c). At these temperatures the circulation is driven by meltwater rather than dense rejected brine, and this can be seen by the presence of slightly cooler meltwater along the sides and top of the crevasse. In the colder case (Figure 7d) the contours are sloped, with colder water rising up the downstream side of the crevasse. The warmer, dense water produced by freezing can be seen descending down the upstream side. Significant amounts of supercooled water are in contact with the ice high up the downstream side and at the top of the crevasse, leading to freezing there (Figure 8a). In melt-dominated cases, such as $T2$, a higher proportion of the freeze rate results from direct freezing than deposition of frazil ice (Table 1).

4.3. Velocity Variation

Greater inflow velocities were found to create a stronger overturning circulation within the crevasse, due to the increased meltwater supply from outside the crevasse and the shear of the flow past the crevasse bottom. While the freezing rate generally increases with velocity, the overall magnitude remains largely the same (Figure 8b). As the freezing rate is dominated by frazil ice production rather than direct freezing the velocity-driven increase in direct freezing is weak. The circulation in the crevasse is buoyancy driven, and while increasing the inflow velocity does increase melting outside the crevasse, and therefore the buoyancy, this has little effect on the flow in the crevasse.

4.4. Frazil Crystal Size Variation

Even with no freezing or melting in the model at all there is still a circulation driven by the shear past the crevasse (Figure 9a), although this circulation is an order of magnitude slower

Table 1. Average Freezing Rate and Frazil Ice Contribution to Freezing Rate for the Baseline, $T2$ (Warmer Than Baseline), $T4$ (Colder Than Baseline), $R025$ (Smaller Radii Than Baseline), and $R150$ (Larger Radii Than Baseline)[a]
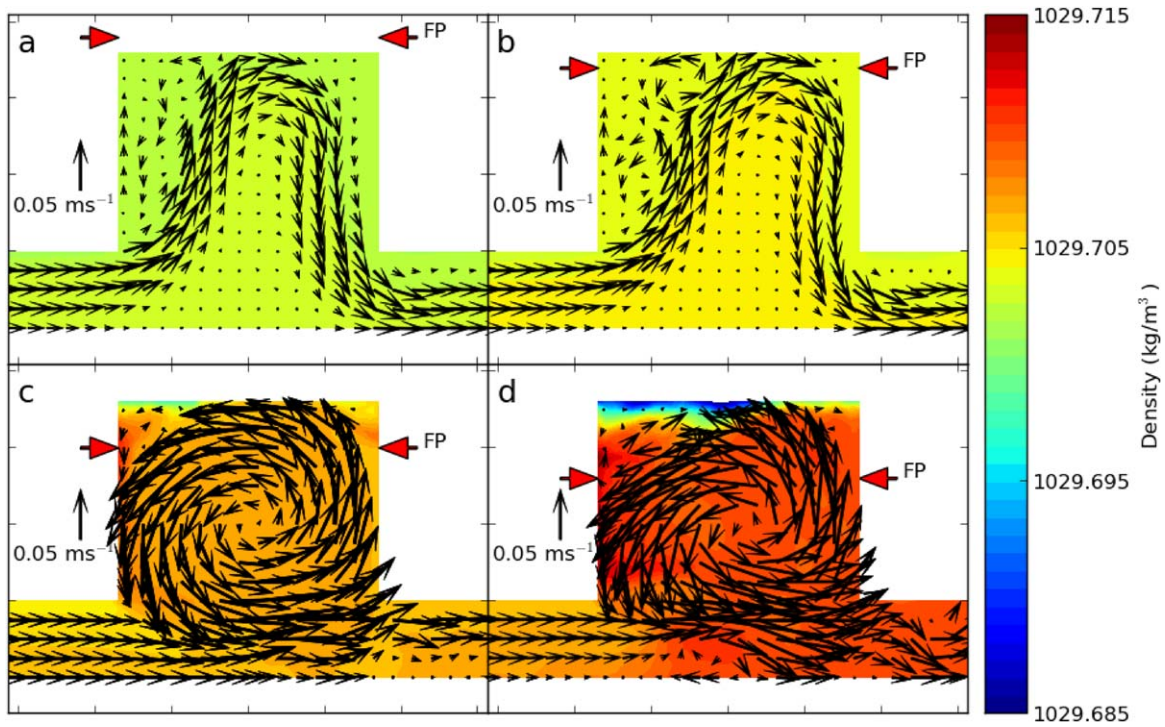
Run	Average Freezing Rate (m/a)	Frazil Ice Percentage Contribution
Baseline	8.32	97.8
$T2$ (warm)	0.05	1.7
$T4$ (cold)	31.8	99.7
$F025$ (small crystal radii)	5.81	99.9
$F150$ (large crystal radii)	0.06	3.3

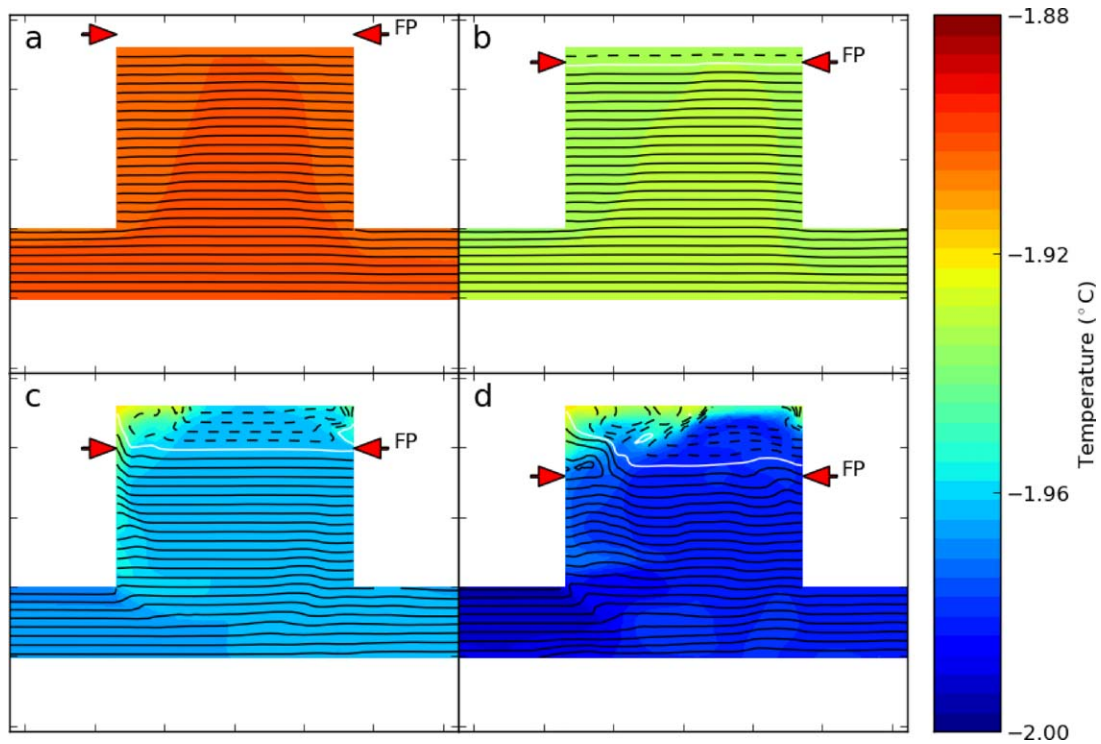[a]Freezing rates are spatially averaged over the top of the crevasse.

Figure 6. Mean density with mean velocity vectors for the inflow temperatures (a) $T1$, (b) $T2$, (c) $T3$ (baseline), and (d) $T4$. The pressure-dependent FP of the four different inflow temperatures is also shown.

Figure 7. Mean temperature (colors) with thermal driving (contours) for the inflow temperatures (a) $T1$, (b) $T2$, (c) $T3$, and (d) $T4$. The white contour is at thermal driving equal to 0, while black contours are every $0.1°$ above and black dashed contours are every $0.01°$ below this point.
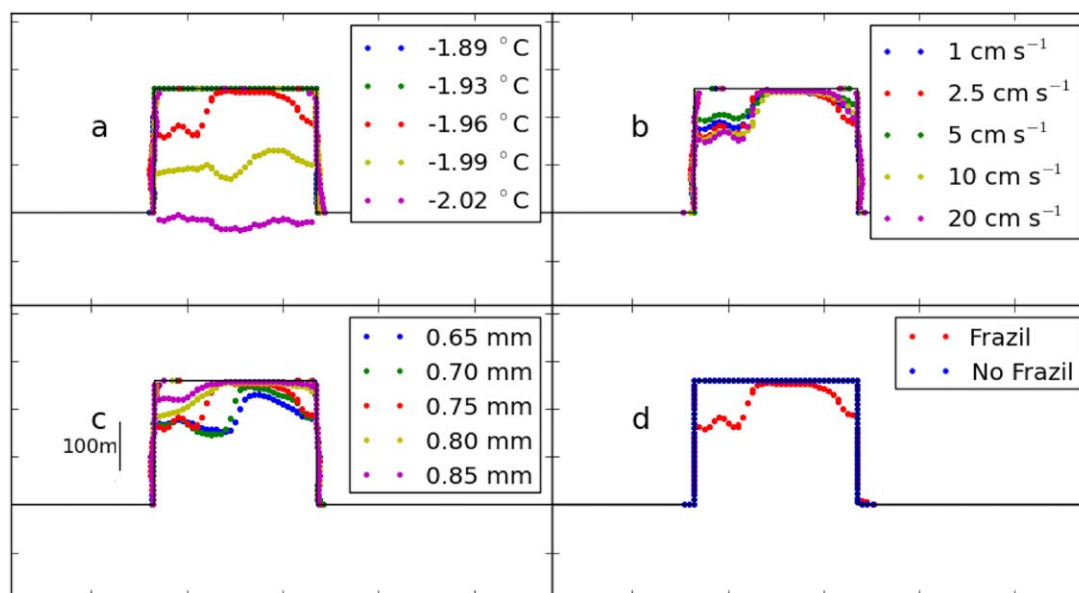
Figure 8. Change in crevasse geometry as a result of averaged melt rate maintained for 10 years for (a) temperature variation of inflow water, (b) velocity variation of inflow water, (c) variation in frazil crystal radii, and (d) effect of no-frazil component in the model. An increase in crevasse size represents melting, while a decrease represents freezing.

than the inflow velocity and is negligible when compared with the baseline case (Figure 9d). When only direct melting and freezing are used (Figure 9b) the crevasse hosts a large amount of supercooled water, as direct freezing is too slow to quench the supercooling (Figure 10a). As only a small amount of freezing is occurring we see a similar melt-driven flow pattern as with warmer temperatures (Figure 9b), with only a hint of the brine-driven recirculation.

When frazil melting and freezing is activated, varying the size of frazil crystals dramatically changes the rate at which supercooling is quenched in the crevasse, and hence the amount of dense water production. Smaller crystals freeze faster due to their larger surface area per unit volume. For extremely small crystals, this has the effect of removing virtually all supercooling from the water column (Figure 10b, $r = 0.25$ mm). Crucially, however, the smaller crystals have a very low rising velocity, so they remain in suspension and lower the density of the mixture (Figure 9c). Larger crystals form at a slower rate, and so more supercooling is present in the crevasse; thermal driving contours are flat and resemble the no-frazil case (Figure 10d, $r = 1.5$ mm). Brine production slows down and the circulation returns to the meltwater-driven flow seen in other cases with low freezing rates.

It is important to note that the frazil radii used in Figures 9 and 10 are at the extreme ends of the range of radii observed in laboratory experiments [*Clark and Doering*, 2006] and are shown for illustrative purposes only. Our model requires a single representative crystal radius, and these extreme values will never be representative of the entire frazil population. *Clark and Doering* [2006] show that 0.5–1 mm might be a more suitable range of representative radii. When the frazil crystal radius is varied by a smaller amount around the baseline value the general, asymmetric pattern of freezing remains the same, although with a flattening of the spatial distribution (Figure 8c). With smaller radii frazil ice is produced quicker, increasing deposition on the downstream side, while the slower forming larger radii deposit less on the upstream side. Once again, the freezing rate in freeze-dominated cases (low to medium crystal radii) is dominated by frazil ice precipitation, while melt-driven cases (high crystal radii) are dominated by direct freezing (Table 1).

4.5. Crevasse Geometry Variation

If the width of the crevasse is larger than its height the crevasse is sufficiently shallow that it is not permitted to generate its own independent circulation (Figure 11a). If the crevasse is much taller than its width, several counter-rotating circulations can form on top of each other (Figure 11b). Extending the depth of the cavity below the ice shelf (Figure 11c) has little effect on the qualitative nature of the flow field. A triangular-shaped crevasse (Figure 11d) sees a weaker freeze-driven overturning circulation, due
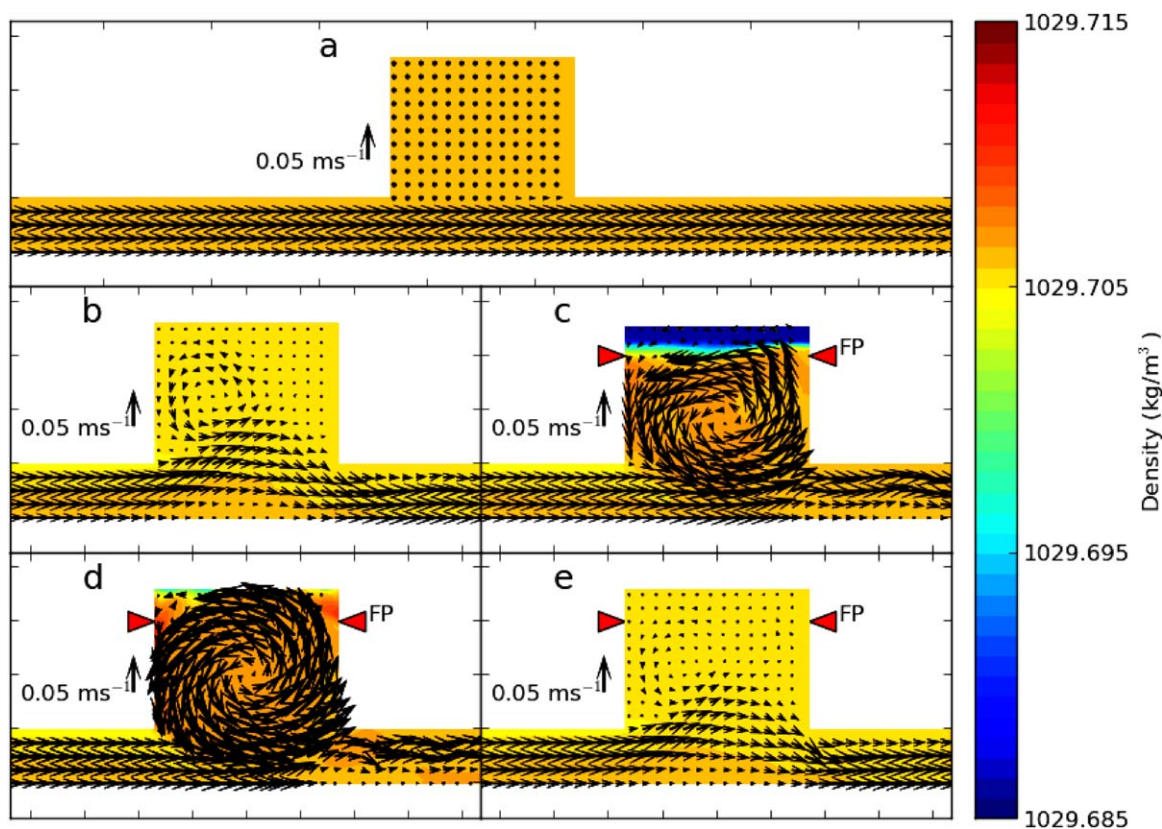
Figure 9. Time-averaged mean density with time-averaged mean velocity vectors for (a) the no-melting case, (b) the no-frazil case, (c) $R025$, (d) $R075$ (baseline), and (e) $R150$.

to the narrowing of the crevasse reducing the total amount of supercooled water present at the top of the crevasse.

5. Discussion

This modeling study demonstrates that ocean circulation in ice-shelf basal crevasses takes two main forms, one driven by freezing and one by melting. In the first the flow is driven by freezing and brine rejection at the top of the crevasse, creating unstable stratification that leads to a density-driven overturning circulation. The second form is primarily driven by melting, with buoyant meltwater from outside the crevasse rising along the sides and top of the crevasse. Which circulation is present is determined by the amount of freezing taking place in the crevasse, with the melt-driven circulation for low amounts of freezing and the freezing-driven case otherwise. In the absence of melting and freezing there is essentially no flow in the crevasse.

Freezing within a crevasse is dominated (roughly 99% in the baseline case) by frazil ice precipitation rather than direct freezing. Frazil ice formation is largely determined by ocean temperature and crystal radius, with higher ocean velocities providing only a small increase in freezing. Future modeling studies of ice shelves with basal crevasses therefore need to be aware of the crucial role played by frazil ice.

The results of an ocean-temperature sensitivity study show a highly nonlinear relationship between the "far-field" temperature and the overall freezing rate. The freezing rate for the coldest cases is so large, several tens of meters per year, that any crevasse with this amount of supercooled water will quickly fill in with marine ice and thus limit the amount of supercooling present. As such we would expect it to be highly unlikely for a crevasse to have much more than the observed 60 m of supercooling. This could also explain the rapid initial decrease in crevasse depth as they propagate toward the calving front seen by *Luckman*
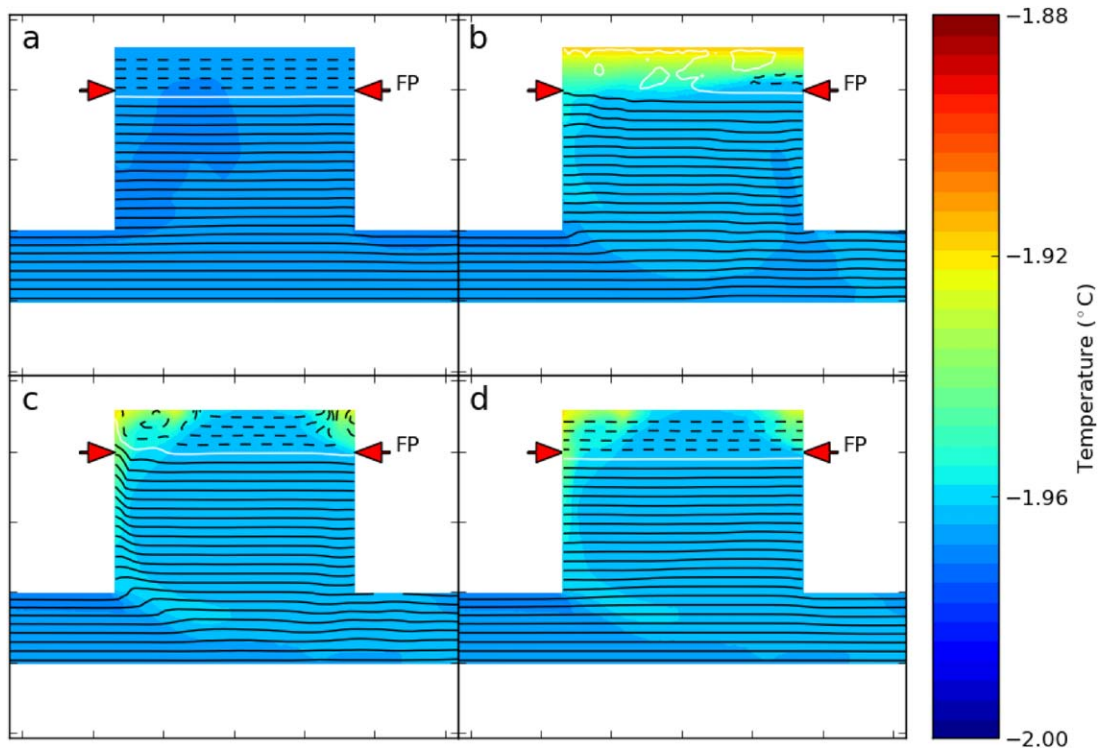
Figure 10. Mean temperature (colors) with thermal driving (contours) for (a) the no-frazil case, (b) *R*025, (c) *R*075 (baseline), and (d) *R*150. The white contour is at thermal driving equal to 0, while black contours are every 0.1° above and black dashed contours are every 0.01° below this point.

et al. [2012], assuming that the thermal driving is roughly uniform. This sensitivity to temperature change is highly asymmetric, with a very small cooling filling a crevasse with marine ice, but a reversal of that cooling would take decades to melt the marine ice.

Our model makes a number of assumptions for the sake of computational simplicity and to provide a first example of a previously unstudied process. In our model the frazil crystal radius is limited to a single
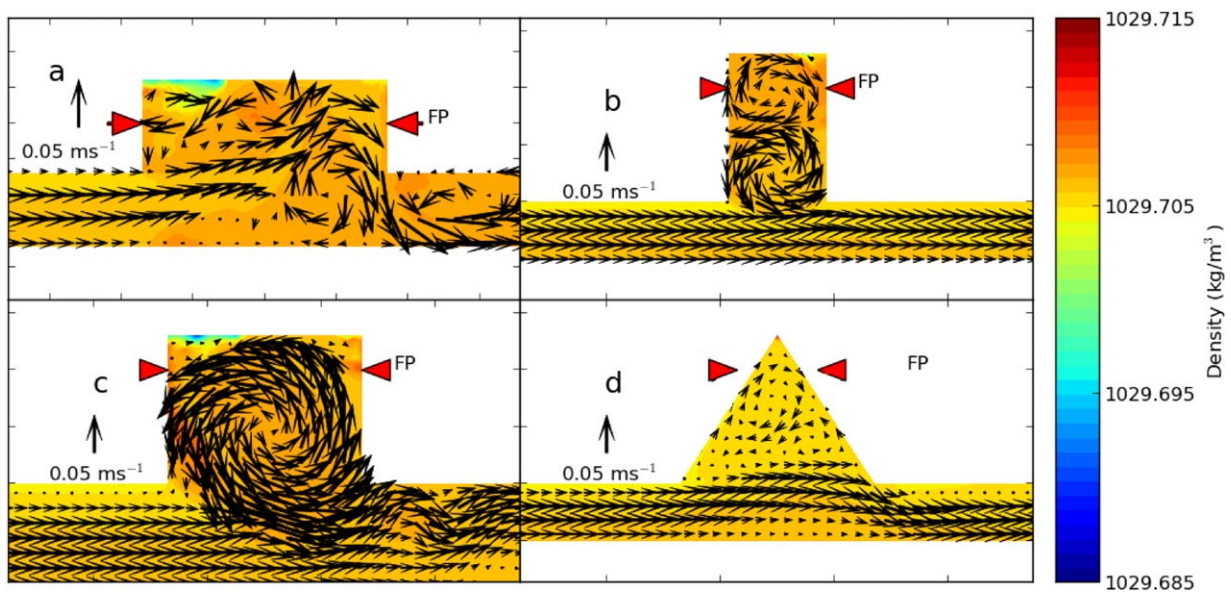
Figure 11. Mean density with mean velocity vectors for different crevasse geometries: (a) 260 m wide and 170 m deep, (b) 130 m wide and 340 m deep, (c) cavity extended to 200 m deep, and (d) cavity extended to 500 m deep.

"representative" value, whereas in reality individual crystals will grow and shrink in size. Incorporating multiple size frazil crystals into our model [*Smedsrud and Jenkins*, 2004; *Holland and Feltham*, 2005; *Galton-Fenzi et al.*, 2012] would therefore be a logical next step. It is also possible that the overturning circulation within the crevasse is partly caused by the 2-D nature of the model used here, and so a 3-D model would allow us to investigate this, as well as the effect of the Coriolis force. The 2-D nature of our model also limits us to studying large-scale flows perpendicular to crevasses, when in reality the flow past the crevasse could be oriented in any direction. Despite these limitations we feel our model can provide important new insights into ice-ocean interaction and ocean flow in ice-shelf crevasses.

6. Conclusions

We have used an advanced ocean model to study the circulation and ice-ocean interaction in an idealized, 2-D ice-shelf basal crevasse. We draw the following conclusions:

1. Circulation within a crevasse is highly dependent upon the amount of freezing. Two different circulation patterns are found, one freeze dominated and one melt dominated. In the first an unstable overturning circulation is formed due to dense water formation at the top of the crevasse, while in the second a stable meltwater layer is formed along the sides and top of the crevasse.

2. Frazil ice precipitation is the dominant factor in the freeze rate within basal crevasses, providing roughly 99% of the freeze rate in our baseline case. At lower amounts of supercooling direct freezing becomes more important, although frazil ice precipitation is still the prime means of freezing.

3. Freezing in the crevasse is primarily dependent upon the temperature of the inflow water and the chosen size of the model's "representative" frazil crystal radius, with inflow velocity having a much smaller effect. There is a nonlinear relationship between inflow temperature and freezing rate, with temperatures 0.03°C colder than our baseline case quickly approaching freezing rates of 50 m a year. As such, we consider it highly unlikely that much more than 60 m of supercooling would be present in a basal crevasse, as otherwise it would quickly fill with marine ice. The rapid freezing permitted by frazil ice creates a strong asymmetry where crevasses can fill with marine ice after a cooling far more rapidly then the marine ice would be eroded after a similar warming.

Freezing in ice-shelf crevasses provides a strong stabilizing influence on ice shelves underlain by cold water that is not found elsewhere.

References

Clark, S., and J. Doering (2006), Laboratory experiments on frazil-size characteristics in a counterrotating flume, *J. Hydraul. Eng.*, *132*(1), 94–101, doi:10.1061/(ASCE)0733-9429(2006)132:1(94).

Cook, A. J., and D. G. Vaughan (2010), Overview of areal changes of the ice shelves on the Antarctic Peninsula over the past 50 years, *Cryosphere*, *4*, 77–98.

Cotter, C. J., D. A. Ham, C. C. Pain, and S. Reich (2009), LBB stability of a mixed Galerkin finite element pair for fluid flow simulations, *J. Comput. Phys.*, *228*(2), 336–348, doi:10.1016/j.jcp.2008.09.014.

Daly, S. F. (1984), Evolution of frazil ice in natural water bodies, in *International Association for Hydraulic Research Working Group on Thermal Regimes: Report on Frazil Ice*, edited by S. F. Daly, pp. 19–24, U.S. Army Cold Reg. Res. and Eng. Lab., Hanover, N. H.

Galton-Fenzi, B. K., J. R. Hunter, R. Coleman, S. Marsland, and R. C. Warner (2012), Modelling the basal melting and marine ice accretion of the Amery Ice Shelf, *J. Geophys. Res.*, *117*, C09031, doi:10.1029/2012JC008214.

Glasser, N. F., and T. A. Scambos (2008), A structural glaciological analysis of 2002 Larsen B Ice Shelf collapse, *J. Glaciol.*, *54*, 3–16.

Gosink, J. P., and T. E. Osterkamp (1983), Measurements and analyses of velocity profiles and frazil ice-crystal rise velocities during periods of frazil-ice formation in rivers, *Ann. Glaciol.*, *4*, 79–84.

Hattermann, T., O. A. Nst, J. M. Lilly, and L. H. Smedsrud (2012), Two years of oceanic observations below the Fimbul Ice Shelf, Antarctica, *Geophys. Res. Lett.*, *39*, L12605, doi:10.1029/2012GL051012.

Hellmer, H. H., and S. S. Jacobs (1992), Ocean interactions with the base of Amery Ice Shelf, Antarctica, *J. Geophys. Res.*, *97*(C12), 20,305–20,317, doi:10.1029/92JC01856.

Holland, P. R., and D. L. Feltham (2005), Frazil dynamics and precipitation in a water column with depth-dependent supercooling, *J. Fluid Mech.*, *530*, 101–124.

Holland, P. R., and D. L. Feltham (2006), The effects of rotation and ice shelf topography on frazil-laden ice shelf water plumes, *J. Phys. Oceanogr.*, *36*, 2312–2327, doi:10.1175/JPO2970.1.

Holland, P. R., H. F. J. Corr, D. G. Vaughan, A. Jenkins, and P. Skvarca (2009), Marine ice in Larsen Ice Shelf, *Geophys. Res. Lett.*, *36*, L11604, doi:10.1029/2009GL038162.

Holland, P. R., H. F. Corr, H. D. Pritchard, D. G. Vaughan, R. J. Arthern, A. Jenkins, and M. Tedesco (2011), The air content of Larsen Ice Shelf, *Geophys. Res. Lett.*, *38*, L10503, doi:10.1029/2011GL047245.

Humbert, A., and D. Steinhage (2011), The evolution of the western rift area of the Fimbul Ice Shelf, Antarctica, *Cryosphere*, *5*, 931–944, doi:10.5194/tc-5-931-2011.

Jenkins, A., and A. Bombosch (1995), Modeling the effects of frazil ice crystals on the dynamics of Ice Shelf Water plumes, *J. Geophys. Res.*, *100*(C4), 6967–6981, doi:10.1029/94JC03227.

Jezek, K. C. (1984), A modified theory of bottom crevasses used as a means for measuring the buttressing effect of ice shelves on inland ice sheets, *J. Geophys. Res.*, *89*(B3), 1925–1931, doi:10.1029/JB089iB03p01925.

Jezek, K. C., and C. R. Bentley (1983), Field studies of bottom crevasses in the Ross Ice Shelf, Antarctica, *J. Glaciol.*, *29*, 118–129.

Khazendar, A., and A. Jenkins (2003), A model of marine ice formation within Antarctic ice shelf rifts, *J. Geophys. Res.*, *108*(C7), 3235, doi:10.1029/2002JC001673.

Kimura, S., A. Candy, P. Holland, M. Piggott, and A. Jenkins (2013), Adaptation of an unstructured-mesh, finite-element ocean model to the simulation of ocean circulation beneath ice shelves, *Ocean Modell.*, *67*, 39–51.

Luckman, A., D. Jansen, B. Kulessa, E. C. King, P. Sammonds, and D. I. Benn (2012), Basal crevasses in Larsen C Ice Shelf and implications for their global abundance, *Cryosphere*, *6*(1), 113–123, doi:10.5194/tc-6-113-2012.

McGrath, D., K. Steffen, T. Scambos, H. Rajaram, G. Casassa, and J. L. Rodriguez Lagos (2012a), Basal crevasses and associated surface crevassing on the Larsen C Ice Shelf, Antarctica, and their role in ice-shelf instability, *Ann. Glaciol.*, *53*(60), 10–18, doi:10.3189/2012AoG60A005.

McGrath, D., K. Steffen, H. Rajaram, T. Scambos, W. Abdalati, and E. Rignot (2012b), Basal crevasses on the Larsen C Ice Shelf, Antarctica: Implications for meltwater ponding and hydrofracture, *Geophys. Res. Lett.*, *39*, L16504, doi:10.1029/2012GL052413.

Orheim, O., J. O. Hagen, S. Østerhus, and A. C. Sactrang (1990), Glaciological and oceanographic studies on Fimbulisen during NARE 1989/90, *Filchner-Ronne Ice Shelf Program. Rep.*, *4*, 120–129.

Østerhus, S., and O. Orheim (1992), Studies through Jutulgryta, Fimbulisen in the 1991/92 season, *Filchner-Ronne Ice Shelf Program. Rep.*, *6*, 103–109.

Piggott, M. D., G. J. Gorman, C. C. Pain, P. A. Allison, A. S. Candy, B. T. Martin, and M. R. Wells (2008), A new computational framework for multi-scale ocean modelling based on adapting unstructured meshes, *Int. J. Numer. Methods Fluids*, *56*(8), 1003–1015, doi:10.1002/fld.1663.

Piggott, M. D., P. Farrell, C. Wilson, G. Gorman, and C. Pain (2009), Anisotropic mesh adaptivity for multi-scale ocean modelling, *Philos. Trans. R. Soc. A*, *367*(1907), 4591–4611, doi:10.1098/rsta.2009.0155.

Pritchard, H. D., R. J. Arthern, D. G. Vaughan, and L. A. Edwards (2009), Extensive dynamic thinning on the margins of the Greenland and Antarctic ice sheets, *Nature*, *461*, 971–975, doi:10.1038/nature08471.

Pritchard, H. D., S. R. M. Ligtenberg, H. A. Fricker, D. G. Vaughan, M. R. van den Broeke, and L. Padman (2012), Antarctic ice-sheet loss driven by basal melting of ice shelves, *Nature*, *484*, 502–505, doi:10.1038/nature10968.

Rignot, E., and D. R. MacAyeal (1998), Ice-shelf dynamics near the front of the Filchner-Ronne Ice Shelf, Antarctica, revealed by SAR interferometry, *J. Glaciol.*, *44*, 405–418.

Rignot, E., G. Casassa, P. Gogineni, W. Krabill, A. Rivera, and R. Thomas (2004), Accelerated ice discharge from the Antarctic Peninsula following the collapse of Larsen B Ice Shelf, *Geophys. Res. Lett.*, *31*, L18401, doi:10.1029/2004GL020697.

Rignot, E., S. Jacobs, J. Mouginot, and B. Scheuchl (2013), Ice-Shelf melting around Antarctica, *Science*, *341*(6143), 266–270, doi:10.1126/science.1235798.

Rist, M. A., P. R. Sammonds, H. Oerter, and C. S. M. Doake (2002), Fracture of Antarctic shelf ice, *J. Geophys. Res.*, *107*(B1), ECV 2-1–ECV 2–13, doi:10.1029/2000JB000058.

Robin, G. (1979), Formation, flow and disintegration of ice shelves, *J. Glaciol.*, *24*, 259–271.

Scambos, T. A., C. Hulbe, M. Fahnestock, and J. Bohlander (2000), The link between climate warming and break-up of ice shelves in the Antarctic Peninsula, *J. Glaciol.*, *46*(154), 516–530, doi:10.3189/172756500781833043.

Shepherd, A., D. Wingham, T. Payne, and P. Skvarca (2003), Larsen Ice Shelf has progressively thinned, *Science*, *302*, 856–859.

Smedsrud, L. H., and A. Jenkins (2004), Frazil ice formation in an ice shelf water plume, *J. Geophys. Res.*, *109*, C03025, doi:10.1029/2003JC001851.

Swithinbank, C. (1977), Glaciological research in the Antarctic Peninsula, *Philos. Trans. R. Soc. London B*, *279*(963), 161–183, doi:10.1098/rstb.1977.0080.

Vaughan, D. G., and C. S. M. Doake (1996), Recent atmospheric warming and retreat of ice shelves on the Antarctic Peninsula, *Nature*, *379*, 328–331.